

Cite this: *J. Mater. Chem. A*, 2017, 5, 11016

# Reduced titania@layered double hydroxide hybrid photoanodes for enhanced photoelectrochemical water oxidation†

Jian Guo,<sup>a</sup> Chengyu Mao,<sup>b</sup> Ruikang Zhang,<sup>a</sup> Mingfei Shao,<sup>a\*</sup> Min Wei<sup>a</sup> and Pingyun Feng<sup>b\*</sup>

Photoelectrochemical (PEC) water oxidation has received considerable attention owing to its key role in the overall water splitting. In this work, several reduced titania@layered double hydroxide (CoAl-LDH, CoCr-LDH, and CoFe-LDH) hybrid photoanodes were fabricated *via* electrochemical deposition of LDH on the reduced titania, and their PEC properties for water oxidation were studied systematically. The reduced titania@CoCr-LDH photoanode shows a much improved PEC performance compared with pristine reduced titania, with a photocurrent density enhancement of 43% (from 0.65 mA cm<sup>-2</sup> to 0.93 mA cm<sup>-2</sup>) and an onset potential decrease of 21% (from 0.23 V to 0.18 V vs. the RHE). This improvement is also successfully demonstrated in the reduced titania@CoAl-LDH and reduced titania@CoFe-LDH system. The photoconversion efficiency of reduced titania is significantly enhanced after the incorporation of LDH (0.42–0.51% at ~0.46 V vs. the RHE). Both the experimental studies and DFT calculations confirm a synergistic effect between the reduced titania and LDH. The results show that a good match of the band structure facilitates the fast electron–hole separation and the migration of holes from reduced titania to LDH, followed by the LDH catalyzed water oxidation. The CoCr-LDH has the highest driving force for oxygen evolution among these LDHs, accounting for the optimal PEC performance of the reduced titania@CoCr-LDH photoanode.

Received 23rd January 2017  
Accepted 2nd May 2017

DOI: 10.1039/c7ta00770a

rsc.li/materials-a

## 1. Introduction

Photoelectrochemical (PEC) water splitting under solar irradiation which can convert and store solar energy in the form of hydrogen is receiving considerable attention. The PEC water splitting reaction includes two half reactions, *i.e.* the hydrogen evolution reaction (HER) and oxygen evolution reaction (OER), giving rise to a highly efficient chemical energy in the form of hydrogen and oxygen. However, this overall reaction is kinetically hindered and suffers from a bottleneck from the OER (namely the water oxidation reaction), which involves sequential multiple proton-coupled four-electron transfer (PCET) processes.<sup>1</sup> This has triggered a tremendous effort for seeking a promising way to improve the efficiency of water oxidation in the past few decades. Correspondingly, the design and fabrication of highly efficient and steady photoanodes where the OER takes place are critical for the improvement of the PEC water splitting or oxidation properties.

To date, although many metal oxides have been explored as photocatalysts,<sup>2–4</sup> titanium oxide is still considered as a promising and irreplaceable photocatalyst and photoanode material<sup>5–8</sup> for water splitting since first being reported by Fujishima and Honda in 1972.<sup>9</sup> Owing to its poor electrical conductivity, large band gap and the fast recombination of photo-induced carriers, previous efforts have been focused on architectural design,<sup>10–16</sup> doping,<sup>17–19</sup> and incorporation with conductive materials<sup>20–22</sup> or co-catalysts.<sup>23,24</sup> In addition, a novel method to grow titanium oxide nanorods directly on a flexible Ti foil was demonstrated. The nanorods could be further reduced by hydrazine leading to the formation of high Ti<sup>3+</sup> self-doped titania. The resulting photoanode material exhibits significantly improved PEC activity owing to an enhanced donor density resulting from the abundant Ti<sup>3+</sup> and thus higher electronic conductivity.<sup>25</sup> However, if the transport or transfer of the photoexcited carriers is insufficient, the oxygen vacancies resulting from Ti<sup>3+</sup> doping may become new recombination sites for electron–hole pairs within the bulk.<sup>26</sup>

Layered double hydroxides (LDHs) have been explored as the precursors of catalysts, photocatalysts or photoelectrocatalysts for the degradation of organic dyes and pollutants,<sup>27–34</sup> as well as for water splitting or oxidation reactions since Garcia *et al.* reported the photocatalytic OER activity of several LDHs (*i.e.*, ZnTi-, ZnCe- and ZnCr-LDH) under visible light.<sup>35</sup> Subsequently, titanium-

<sup>a</sup>State Key Laboratory of Chemical Resource Engineering, Beijing University of Chemical Technology, Beijing 100029, P. R. China. E-mail: shaomf@mail.buct.edu.cn

<sup>b</sup>Department of Chemistry, University of California, Riverside, CA 92521, USA. E-mail: pingyun.feng@ucr.edu

† Electronic supplementary information (ESI) available. See DOI: 10.1039/c7ta00770a

embedded LDHs,<sup>36–38</sup> cobalt-based LDHs,<sup>39</sup> zinc-containing LDHs<sup>40,41</sup> and chromium-containing LDHs<sup>42–45</sup> have attracted extensive attention as photocatalysts toward the water splitting reaction. However, the photocatalytic and PEC activities of LDHs are far from satisfactory; as a result, LDHs combined with titanium oxide,<sup>22–24</sup> zinc oxide,<sup>46,47</sup> iron oxide,<sup>48–50</sup> tantalum nitride,<sup>51</sup> cuprous oxide,<sup>52</sup> cadmium sulfide,<sup>53</sup> cadmium telluride<sup>54</sup> and bismuth vanadate<sup>55</sup> have also been intensively investigated for the photocatalytic or photoelectrochemical reactions. Our group has carried out studies on LDHs toward photocatalytic and PEC water splitting.<sup>22,56</sup> Theoretical calculations revealed that the band structures of several transitional metal-containing LDHs are suitable for the OER, and the photoinduced holes localized on the surface hydroxyl group of LDHs can facilitate the oxidization of water molecules.<sup>57</sup>

Based on the previous work, herein, we fabricated several hybrid photoanodes consisting of reduced titania and modified LDHs (CoAl-LDH, CoCr-LDH and CoFe-LDH). It is expected that the synthesized hybrid photoanode materials with suitable band structures could facilitate charge separation, hole transfer and water oxidation catalysis. Our experimental results show that the modified hybrid photoanode with CoCr-LDH has a much enhanced current density, increasing 43% compared with the pristine reduced titania photoanode. A further insight into the mechanism toward the enhanced PEC water oxidation was discussed according to both experimental study and theoretical calculation. A synergistic effect between reduced titania and LDH plays a key role in the enhanced PEC water oxidation performance: the higher driving force in the reduced titania@CoCr-LDH system is responsible for improving the separation and transfer of holes while the co-catalytic effect of LDH can increase the utilization efficiency of holes and suppress the recombination of generated electron-hole pairs.

## 2. Experimental section

### 2.1. Preparation of the reduced titania@LDH hybrid photoanode

The titanium foil (0.25 mm thickness, 99.7% trace metal) and metal salt were purchased from Sigma-Aldrich Co. LLC (USA). The bare reduced titania (*i.e.*, high Ti<sup>3+</sup> self-doped titania) photoanode was grown on titanium foil by a previously reported hydrothermal method.<sup>25</sup> The obtained sample was labeled as Ti-TiO<sub>2-x</sub>.

The LDH was deposited onto Ti-TiO<sub>2-x</sub> through a potentiostatic deposition method by using an electrochemical workstation (CHI 660C, CH Instrument Co. USA). The obtained Ti-TiO<sub>2-x</sub> was used as the working electrode and placed in an electrochemical cell, which was assembled in a three-electrode configuration, with a platinum foil as the counter electrode and an Ag/AgCl as the reference electrode. The electrolyte for electrodeposition of CoAl-LDH was a mixed solution of CoCl<sub>2</sub>·6H<sub>2</sub>O (0.1 M) and Al(NO<sub>3</sub>)<sub>3</sub>·9H<sub>2</sub>O (0.1 M). The potentiostatic deposition was carried out at a potential of -1.0 V *vs.* Ag/AgCl. The resulting hybrid composite (denoted as Ti-TiO<sub>2-x</sub>@CoAl-LDH) was recovered and rinsed thoroughly with distilled water and absolute ethyl alcohol, followed by drying in an Ar stream.

The preparations of Ti-TiO<sub>2-x</sub>@CoCr-LDH and Ti-TiO<sub>2-x</sub>@CoFe-LDH were similar to the above synthetic procedures, except that the electrolyte was the mixture of CoCl<sub>2</sub>·6H<sub>2</sub>O (1.0 mM) and Cr(NO<sub>3</sub>)<sub>3</sub>·6H<sub>2</sub>O (1.0 mM) for Ti-TiO<sub>2-x</sub>@CoCr-LDH, and CoCl<sub>2</sub>·6H<sub>2</sub>O (1.0 mM) and FeSO<sub>4</sub>·6H<sub>2</sub>O (1.0 mM) for Ti-TiO<sub>2-x</sub>@CoFe-LDH. All the samples with and without LDH modification were used as photoanodes for evaluating PEC water oxidation performance.

### 2.2. Characterization

Powder X-ray diffraction patterns of the samples were collected on a Bruker D8 Advance powder diffractometer operating at 40 kV, 40 mA for Cu K<sub>α</sub> radiation ( $\lambda = 1.54 \text{ \AA}$ ) using a Cu K<sub>α</sub> source, with a scan step of 0.02° and a scan range between 5° and 80°. The UV-Visible Diffuse Reflectance Spectra were recorded on a Shimadzu UV-3101PC UV-Vis-NIR Spectrophotometer. ESR data were measured at 90 K on an ESP300E Electron Spin Resonance Spectrometer, Bruker. The other tests, such as SEM, EDX mapping, HRTEM, XPS, and so on, were similar to the previous work of our group.<sup>22</sup>

### 2.3. Photoelectrochemical and electrochemical measurements

Photoelectrochemical measurements were performed on a Solartron 1287 electrochemical interface analysis instrument operated with the CorrWare program in a standard three-electrode configuration. The fabricated samples were used as photoanodes with an illumination area of ~0.54 cm<sup>2</sup>. The Pt foil and Ag/AgCl electrode were used as the counter and reference electrodes, respectively. Measurements were performed in 1.0 M KOH (pH = 13.6) purged with Ar as the supporting electrolyte medium. The measured potentials *vs.* Ag/AgCl were converted to the reversible hydrogen electrode (RHE) scale *via* the Nernst equation  $E_{\text{RHE}} = E_{\text{Ag/AgCl}} + 0.197 + 0.059 \times \text{pH}$ . A 150 W xenon lamp (Newport, 69907) coupled with an AM 1.5G filter (Newport, 81094) was applied as the simulated sunlight source, and the incident light illuminated from the front side of the photoanode. The light intensity was adjusted to 100 mW cm<sup>-2</sup> with a radiant power meter (Newport, 70260) combined with a probe (Newport, 70268). The measurement of photoelectrochemically generated O<sub>2</sub> was carried out in a home-made airtight transparent electrochemical cell (see detailed description in the ESI†). The incident photon to current efficiency (IPCE) was measured under the same xenon lamp equipped with a monochromator (Newport, 74404).

Electrochemical impedance spectroscopy (EIS) was carried out using a Solartron 1260 impedance analyzer in the frequency range of 10<sup>5</sup> to 10<sup>-1</sup> Hz with an AC voltage amplitude of 50 mV. A DC bias of open circuit potential was applied to each sample in the dark or under illumination. Mott-Schottky measurements were performed with a voltage of 50 mV at a frequency of 5 kHz under dark conditions. IPCE can be calculated by the equation  $\text{IPCE} = (1240 \times J) / (\lambda \times P_{\text{light}})$ , where  $J$  is the measured photocurrent density (mA cm<sup>-2</sup>) at a specific wavelength,  $\lambda$  is the wavelength (nm) of incident light, and  $P_{\text{light}}$  is the measured irradiance (mW cm<sup>-2</sup>) at a specific wavelength.

### 3. Results and discussion

#### 3.1. Structural characterization

Reduced titania grown on a Ti foil substrate ( $\text{Ti-TiO}_{2-x}$ ) has been synthesized based on the reported method,<sup>25</sup> with a diameter distribution from tens to hundreds of nanometers (Fig. S1A†). A strong ESR signal of self-doped  $\text{Ti}^{3+}$  in the reduced titania photoanode is observed, indicating the presence of  $\text{Ti}^{3+}$  (Fig. S1B†). The LDHs were *in situ* electrosynthesized on the surface of  $\text{Ti-TiO}_{2-x}$ .<sup>22</sup> The loading amount of LDH on  $\text{Ti-TiO}_{2-x}$  was controlled by electrodeposition time (the as-synthesized sample is denoted as  $\text{Ti-TiO}_{2-x}@\text{LDH-}t$ ;  $t$  is the deposition time). As shown in Fig. 1, the XRD patterns of  $\text{Ti-TiO}_{2-x}@\text{LDHs-300s}$  show the superimposition of both a rutile phase and an LDH phase. More specifically, besides the peaks of Ti foil (JCPDS: 44-1294), the peaks located at  $27^\circ$ ,  $36^\circ$ ,  $39^\circ$ ,  $41^\circ$ ,  $54^\circ$ ,  $63^\circ$  and  $76^\circ$  are observed and can be indexed to the (110), (101), (200), (111), (211), (002) and (202) lattice diffractions of rutile titanium oxide (JCPDS: 21-1276), while the typical (003) reflections of LDH are clearly observed near  $11^\circ$  for both  $\text{Ti-TiO}_{2-x}@\text{CoAl-LDH-300s}$  and  $\text{Ti-TiO}_{2-x}@\text{CoCr-LDH-300s}$ . And for  $\text{Ti-TiO}_{2-x}@\text{CoFe-LDH-300s}$ , the peak is close to  $10^\circ$ . The SEM images of  $\text{Ti-TiO}_{2-x}@\text{LDH-300s}$  are shown in Fig. 2A, D and G for CoAl-LDH, CoCr-LDH and CoFe-LDH, respectively. Uniform nanoflakes of LDH are formed on the surface of  $\text{Ti-TiO}_{2-x}$ , and the structure of the reduced titania core with an LDH shell can be obviously observed. We further investigated the  $\text{Ti-TiO}_{2-x}@\text{LDH}$  with shorter deposition time. For the  $\text{Ti-TiO}_{2-x}@\text{LDH-40s}$  photoanode, no visible morphology or LDH diffraction could be observed from either SEM images (Fig. 2B, E and H) or XRD patterns (Fig. S2†). However, the EDX mappings confirm the existence and uniformity of LDH. The HRTEM images also indicate the hybrid structures. A very thin (no more than 10 nm) overlayer on bare  $\text{Ti-TiO}_{2-x}$  photoanodes for  $\text{Ti-TiO}_{2-x}@\text{CoAl-LDH-40s}$ ,  $\text{Ti-TiO}_{2-x}@\text{CoCr-LDH-40s}$  and  $\text{Ti-TiO}_{2-x}@\text{CoFe-LDH-40s}$  can be clearly observed (Fig. 2C, F and I). Furthermore, Fig. 2C shows the lattice fringes

corresponding to the interplanar distance of  $\sim 0.22$  and  $\sim 0.32$  nm, which can be attributed to the (015) plane of the CoAl-LDH phase and the (110) plane of rutile, respectively. Similarly, the lattice fringes belonging to the CoCr-LDH and CoFe-LDH can also be observed in Fig. 2F and I, respectively.

The surface electron structure and interaction of the hybrid photoanodes were investigated by X-ray photoelectron spectroscopy (XPS). From the Ti 2p XPS spectra (Fig. 3A), with the peaks of  $\text{Ti}^{4+}$  2p<sub>3/2</sub> and  $\text{Ti}^{4+}$  2p<sub>1/2</sub> at 458.5 eV and 464.3 eV, respectively, there are no peaks at 456.6 eV and 461.0 eV for the bare reduced titania (curve a), which can be ascribed to the presence of  $\text{Ti}^{3+}$ .<sup>58,59</sup> Moreover, for the prepared photoanode, taking the reduced titania@CoCr-LDH-40s as an example (curve c in Fig. 3A), the peak of  $\text{Ti}^{4+}$  2p<sub>3/2</sub> is broadened by multiplet splitting effects and can be deconvoluted into another minor peak at 458.2 eV, resulting from the interaction between the reduced titania and CoCr-LDH. This negative shift of the binding energy suggests an increase in the electron density of the reduced titania, which gives the migration of photo-generated electrons from LDH to reduced titania.<sup>23</sup> Similar results can be obtained from the curves b and d (for  $\text{Ti-TiO}_{2-x}@\text{CoAl-LDH-40s}$  and  $\text{Ti-TiO}_{2-x}@\text{CoFe-LDH-40s}$ , respectively). On the other hand, the O 1s XPS spectra (Fig. 3B) were used to gain further insight into the interaction between the reduced titania and CoCr-LDH. It is obviously found that there is a prominent peak at 529.7 eV for all the samples, which belongs to the oxygen atom in the lattice of reduced titanium oxide.<sup>60</sup> The difference between the bare photoanode (curve a) and the hybrid photoanodes (curves b, c and d) is that a weak peak can be observed at 532.1 eV for the  $\text{Ti-TiO}_{2-x}@\text{CoAl-LDH-40s}$ , or at 531.6 eV for both  $\text{Ti-TiO}_{2-x}@\text{CoCr-LDH-40s}$  and  $\text{Ti-TiO}_{2-x}@\text{CoFe-LDH-40s}$ . It is reported that these weak peaks are attributed to the oxygen of metal hydroxide which comes from LDH.<sup>22</sup> Furthermore, the electron structures of cobalt in LDH were simultaneously collected (Fig. S3†). For example, the reduced titania@CoCr-LDH-40s shows two prominent peaks of Co 2p<sub>3/2</sub> and Co 2p<sub>1/2</sub> at 781.0 and 796.0 eV (Fig. S3B†), and the binding energy of Co 2p<sub>3/2</sub> can be deconvoluted into 780.0 and 781.5 eV, suggesting the coexistence of  $\text{Co}^{3+}$  2p<sub>3/2</sub> and  $\text{Co}^{2+}$  2p<sub>3/2</sub> oxidation states. And the  $\text{Co}^{3+}$  2p<sub>3/2</sub> is also present in the  $\text{Ti-TiO}_{2-x}@\text{CoAl-LDH-40s}$  and the  $\text{Ti-TiO}_{2-x}@\text{CoFe-LDH-40s}$  according to Fig. S3A and S3C.† The presence of  $\text{Co}^{3+}$  illustrates the co-catalytic effect of LDH because  $\text{Co}^{2+}$  can be oxidized to  $\text{Co}^{3+}$  by photo-generated holes, leading to water molecular oxidation simultaneously by  $\text{Co}^{3+}$  and photoinduced holes.

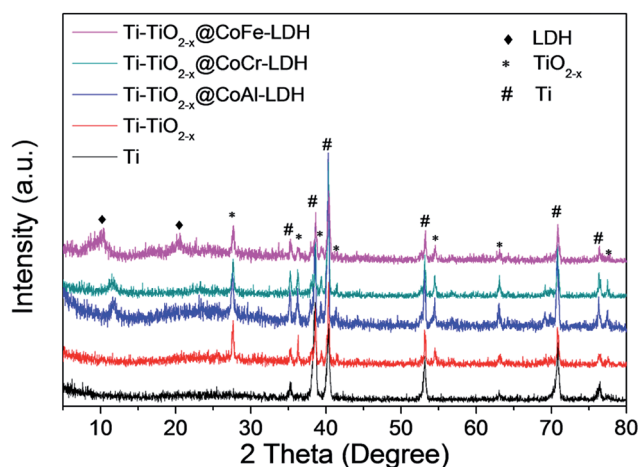


Fig. 1 XRD patterns of Ti foil,  $\text{Ti-TiO}_{2-x}$ ,  $\text{Ti-TiO}_{2-x}@\text{CoAl-LDH}$ ,  $\text{Ti-TiO}_{2-x}@\text{CoCr-LDH}$  and  $\text{Ti-TiO}_{2-x}@\text{CoFe-LDH}$ .

#### 3.2. Optical properties

Fig. 4A–C show the light absorbance of all the photoanodes by using UV-vis diffuse reflectance spectroscopy. The corresponding insets were the Tauc plots of the corresponding samples, which were used to calculate the band gap. The bare  $\text{Ti-TiO}_{2-x}$  exhibits a strong absorption at 380 nm with its absorption edge extending to 420 nm, which gives a band gap of 3.09 eV, consistent with the reported data.<sup>61,62</sup> All the resulting hybrid photoanodes show small enhancements of the absorbance, and the band gaps are 3.06, 3.07 and 3.06 eV, respectively, for  $\text{Ti-TiO}_{2-x}@\text{CoAl-LDH}$ ,  $\text{Ti-TiO}_{2-x}@\text{CoCr-LDH}$  and  $\text{Ti-TiO}_{2-x}@\text{CoFe-LDH}$ , respectively.

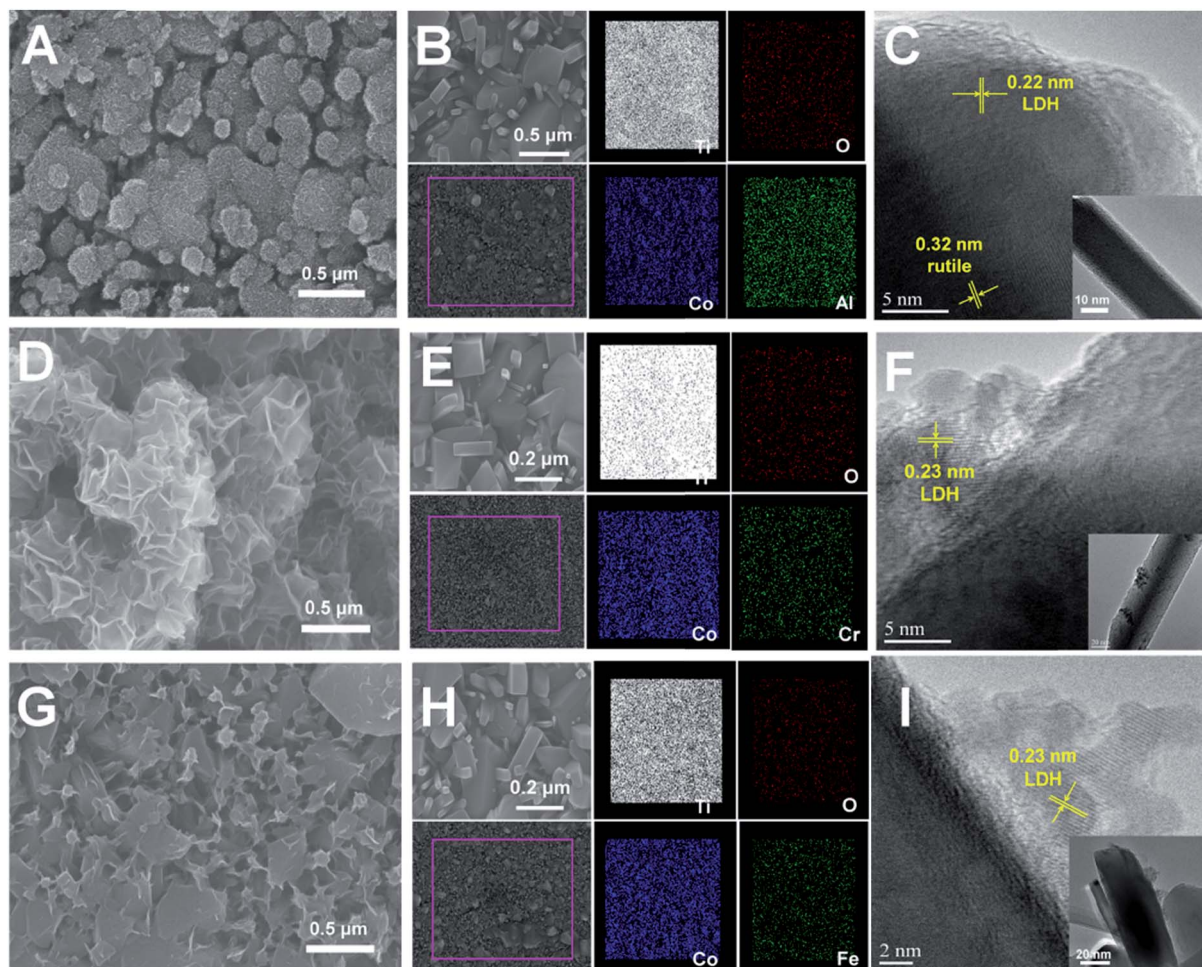


Fig. 2 SEM images of (A)  $\text{Ti-TiO}_{2-x}\text{@CoAl-LDH-300s}$ , (D)  $\text{Ti-TiO}_{2-x}\text{@CoCr-LDH-300s}$  and (G)  $\text{Ti-TiO}_{2-x}\text{@CoFe-LDH-300s}$ ; EDX mappings and typical HRTEM images of (B and C)  $\text{Ti-TiO}_{2-x}\text{@CoAl-LDH-40s}$ , (E and F)  $\text{Ti-TiO}_{2-x}\text{@CoCr-LDH-40s}$ , and (H and I)  $\text{Ti-TiO}_{2-x}\text{@CoFe-LDH-40s}$ .

$\text{TiO}_{2-x}\text{@CoAl-LDH-40s}$ ,  $\text{Ti-TiO}_{2-x}\text{@CoCr-LDH-40s}$ , and  $\text{Ti-TiO}_{2-x}\text{@CoFe-LDH-40s}$ . The slight decrease of the band gap may be owing to the occurrence of a new mid-gap energy level below the conduction band of reduced titania due to the migrated electrons from LDH. This postulate is supported by XPS data. The decrease of the band gap is beneficial for PEC performance. On the other hand, the photoluminescence (PL) behavior can be used to monitor the recombination because it originates from the recombination of photoinduced electron-hole pairs. As a result, the bare reduced titania photoanode displays PL emission peaks between 410 and 490 nm (Fig. 4D). The blue emissions within 410–450 nm are due to the band-band PL phenomenon with the energy of light approximately equal to the band gap energy, while the cyan emissions in the range of 450–490 nm can be ascribed to surface defects.<sup>63,64</sup> After being electrodeposited with LDH, the hybrid photoanode shows a declined PL emission intensity, which indicates that the radiative recombination of photoexcited carrier pairs is effectively suppressed. Especially, the decrease follows a descending order as:  $\text{Ti-TiO}_{2-x}\text{@CoCr-LDH-40s} > \text{Ti-TiO}_{2-x}\text{@CoAl-LDH-40s} > \text{Ti-TiO}_{2-x}\text{@CoFe-LDH-40s}$ . The more significant

suppression can be interpreted as more convenient for charge separation, and thus be more favorable to PEC performance.

### 3.3. Enhancement of PEC performance

The impact of the CoCr-LDH amount on PEC properties was first evaluated by the linear sweep voltammograms (LSVs) under simulated solar radiation (Fig. 5A). At a potential of 1.23 V (*vs.* the RHE), the current density of the bare reduced titania photoanode is  $0.65 \text{ mA cm}^{-2}$ . After electrodeposition for 20 s and 40 s, the current densities of the fabricated hybrid photoanodes of  $\text{Ti-TiO}_{2-x}\text{@CoCr-LDH-20s}$  and  $\text{Ti-TiO}_{2-x}\text{@CoCr-LDH-40s}$  rise to  $0.76 \text{ mA cm}^{-2}$  and  $0.93 \text{ mA cm}^{-2}$ , respectively. However, in the presence of a thicker LDH shell ( $\text{Ti-TiO}_{2-x}\text{@CoCr-LDH-300s}$ ), the photoresponse becomes much weaker compared with the  $\text{Ti-TiO}_{2-x}$  photoanode below 1.1 V (*vs.* the RHE), which is ascribed to the decreased light absorption efficiency of reduced titania with the shielding effect of LDH. This indicates that a moderate deposition of LDH can enhance the PEC performance. In addition, all the hybrid photoanodes show a similar negatively shifted onset potential (from 0.23 to 0.18 V) relative

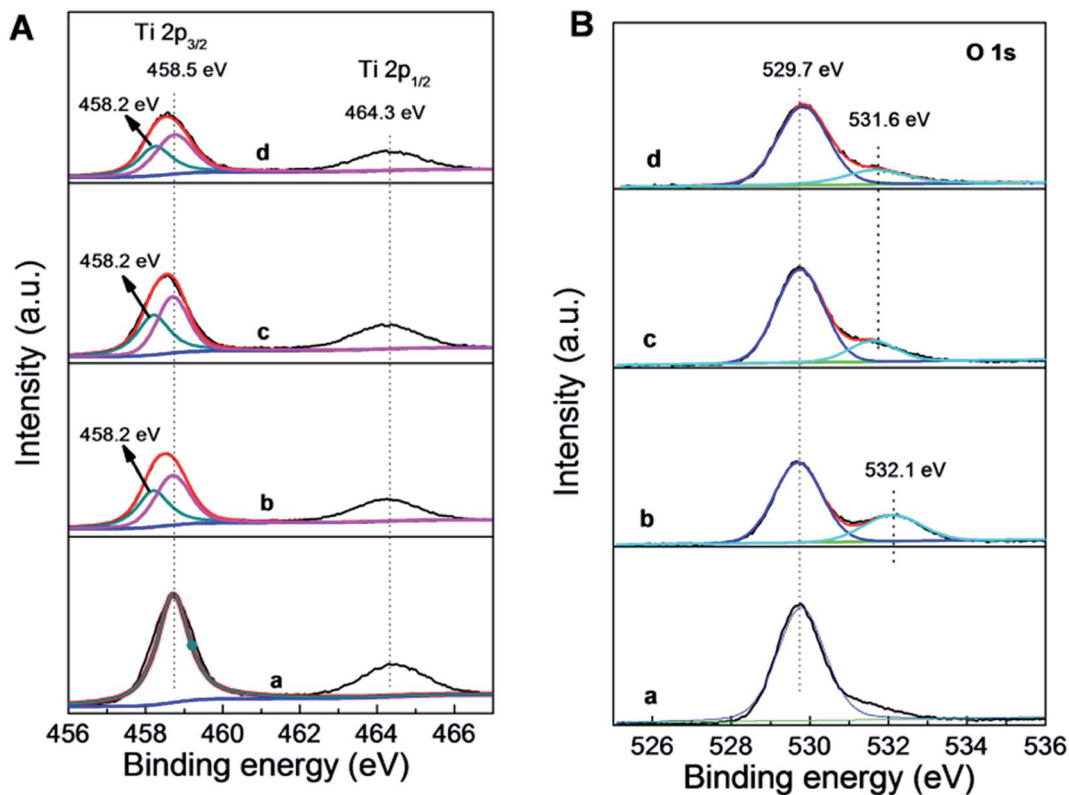


Fig. 3 (A) Ti 2p and (B) O 1s XPS spectra of (a) Ti-TiO<sub>2-x</sub>, (b) Ti-TiO<sub>2-x</sub>@CoAl-LDH-40s, (c) Ti-TiO<sub>2-x</sub>@CoCr-LDH-40s, and (d) Ti-TiO<sub>2-x</sub>@CoFe-LDH-40s, respectively.

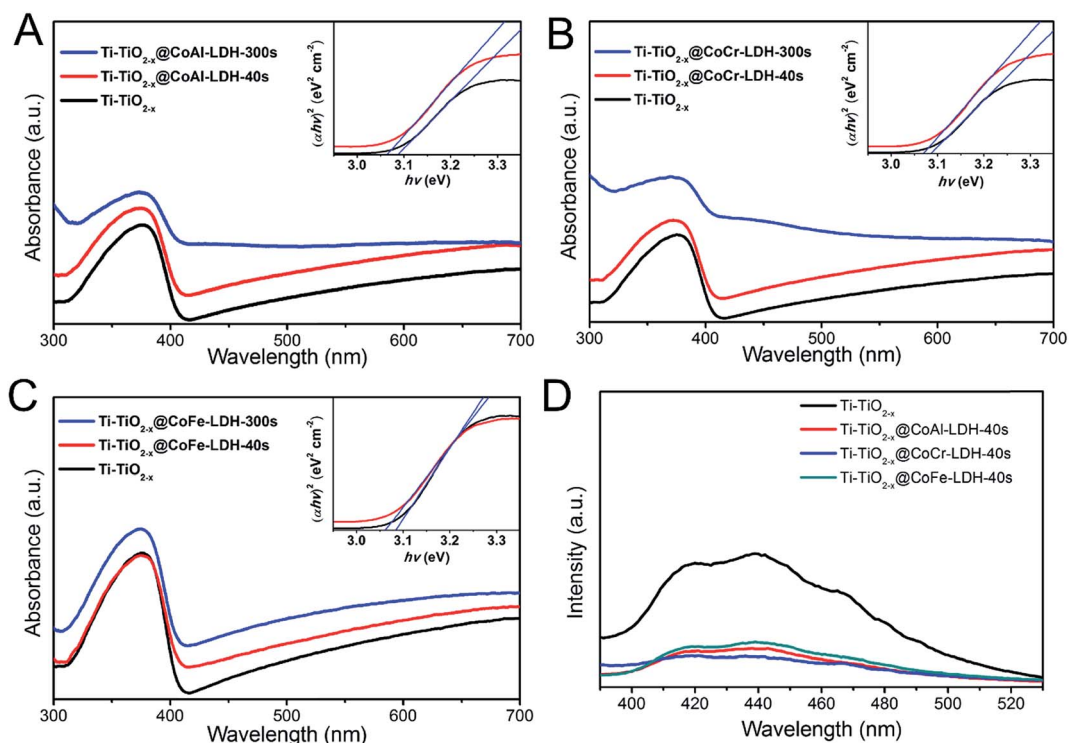


Fig. 4 UV-vis diffuse reflectance spectra and plots (the inset) of  $(\alpha h\nu)^2$  vs.  $h\nu$  of (A) Ti-TiO<sub>2-x</sub>@CoAl-LDH, (B) Ti-TiO<sub>2-x</sub>@CoCr-LDH and (C) Ti-TiO<sub>2-x</sub>@CoFe-LDH, and (D) PL spectroscopy of the photoanodes.

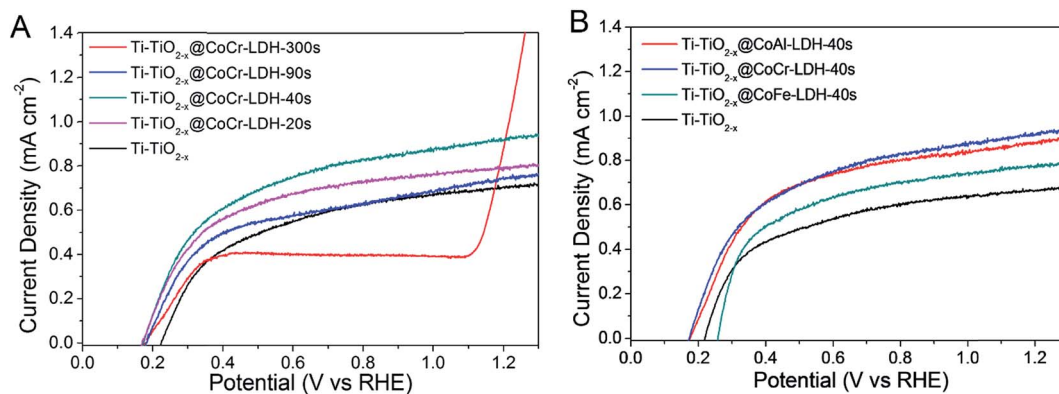


Fig. 5 The comparisons of (A) current–potential ( $J$ – $E$ ) curves of  $\text{Ti-TiO}_{2-x}$ @CoCr-LDH deposited for different times, and (B)  $J$ – $E$  curves under light illumination of  $\text{Ti-TiO}_{2-x}$ @LDH deposited for 40 s with different kinds of LDH (*i.e.* CoAl-LDH, CoCr-LDH and CoFe-LDH).

to the bare one, which can be attributed to the accelerated transport of carriers accumulated on the surface of reduced titania. Furthermore, the influence of different kinds of LDHs (*e.g.* CoCr-LDH, CoAl-LDH, and CoFe-LDH) on PEC properties was also investigated by electrodeposition for 40 s. As shown in Fig. 5B, after electrodeposition with CoAl-LDH and CoFe-LDH, the current densities of these hybrid photoanodes rise to  $0.90 \text{ mA cm}^{-2}$  and  $0.78 \text{ mA cm}^{-2}$  at a bias potential of 1.23 V (*vs.* the RHE). In summary, the current densities of  $\text{Ti-TiO}_{2-x}$ @CoCr-LDH-40s,  $\text{Ti-TiO}_{2-x}$ @CoAl-LDH-40s, and  $\text{Ti-TiO}_{2-x}$ @CoFe-LDH-40s were respectively increased by 43%, 38% and 20% compared to that of  $\text{Ti-TiO}_{2-x}$ , which means that the  $\text{Ti-TiO}_{2-x}$ @CoCr-LDH-40s photoanode has the highest current density for PEC water oxidation among the above four photoanodes. In addition, apart from  $\text{Ti-TiO}_{2-x}$ @CoAl-LDH (Fig. S4A<sup>†</sup>) and  $\text{Ti-TiO}_{2-x}$ @CoFe-LDH (Fig. S4B<sup>†</sup>), the influence of LDH amount for several kinds of LDHs was also systematically surveyed. When the bare photoanode was electrodeposited with CoZn-LDH for 20 s (Fig. S4C<sup>†</sup>), with NiCr-LDH for 20 s (Fig. S4D<sup>†</sup>), with ZnCr-LDH for 60 s (Fig. S4E<sup>†</sup>), or with ZnFe-LDH for 40 s (Fig. S4F<sup>†</sup>), the current densities of these hybrid photoanodes reached the maximum value, and respectively increased by 17%, 50%, 40% and 25% relative to that of the bare photoanode. This shows that the hybrid photoanodes integrated with Cr-based LDHs have a much higher PEC performance toward water oxidation.

The photoconversion efficiency (PcE) is one of the evaluation indexes for the PEC properties of photoanodes and it is a function of photocurrent density and applied bias. The PcE can reach the maximum when enough photocurrent is generated and the applied bias does not negate the advantage of illumination.<sup>25</sup> Both the higher PcE at the same potentials and the smaller value of potential for the maximum PcE are the characters of a better photoanode material. Fig. 6A reveals that the photoconversion efficiency of each photoanode, and the optimal PcE of each photoanode almost appears at 0.46 V (*vs.* the RHE), with the peak values of 0.36%, 0.50%, 0.51% and 0.42% for  $\text{Ti-TiO}_{2-x}$ ,  $\text{Ti-TiO}_{2-x}$ @CoAl-LDH-40s,  $\text{Ti-TiO}_{2-x}$ @CoCr-LDH-40s, and  $\text{Ti-TiO}_{2-x}$ @CoFe-LDH-40s, respectively. These results indicate that  $\text{Ti-TiO}_{2-x}$ @CoCr-LDH-40s has the highest photoconversion efficiency among them. According to Fig. S5A,<sup>†</sup> the maximum PcE of the photoanodes modified with other LDHs (*i.e.* CoZn-, NiCr-, ZnCr- and ZnFe-LDH) is 0.42%, 0.60%, 0.50% and 0.45%, respectively, which also demonstrates that the photoanode modified with Cr-containing LDH has much higher photoconversion efficiency than others.

In order to evaluate the light response promptness and reproduction of the fabricated hybrid photoanode, the transient photocurrents at different bias potentials and at a fixed one of 1.23 V (*vs.* the RHE) were respectively collected by LSV and chronoamperometry under chopped light illumination. Fig. 6B and S5B<sup>†</sup> display that the photocurrents of  $\text{Ti-TiO}_{2-x}$ @LDH

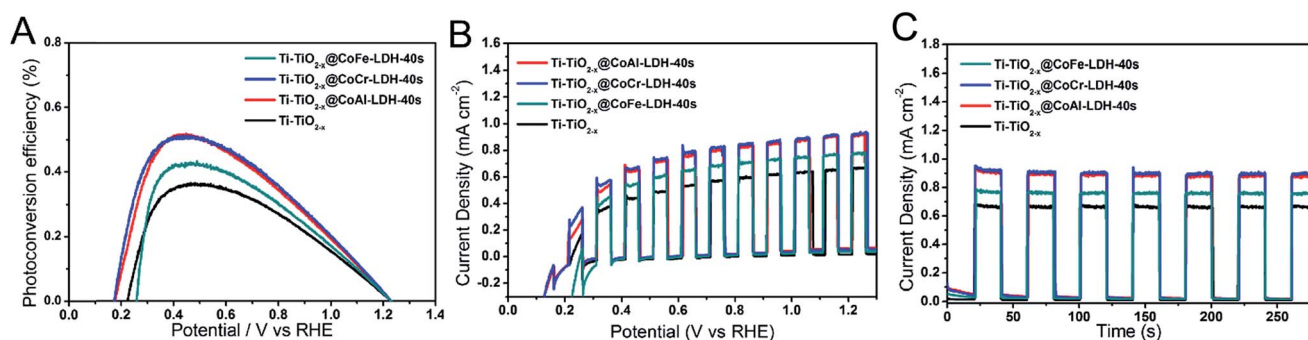


Fig. 6 (A) Calculated photoconversion efficiency, (B)  $J$ – $E$  behavior and (C) amperometric current–time ( $J$ – $T$ ) curves at a potential of 1.23 V (*vs.* the RHE) under chopped light illumination for the samples of  $\text{Ti-TiO}_{2-x}$ @LDH.

photoanodes can rise and fall promptly with increasing bias potential under the conditions of switching on and off of irradiation, which indicates the excellent light response of the hybrid photoanodes. Especially, the  $J$ - $E$  behaviors of all the photoanodes under chopped light irradiation match well with the above results of linear sweep voltammetry (Fig. 5B). Meanwhile, the favorable surface reaction kinetics and the superior reproduction of the hybrid photoanodes can be proved from the square profiles with a steady photocurrent density of the amperometric  $J$ - $T$  curves at a potential of 1.23 V (vs. the RHE) under chopped light illumination (Fig. 6C and S5C†).

Considering the visible light absorbance of  $\text{Ti}^{3+}$ -doped titania and Cr-containing LDH reported before,<sup>35,42,45</sup> we also investigated their PEC performances under visible light ( $\lambda \geq 400$  nm) illumination. As shown in Fig. S5D,† the overall current density and the photocurrent density (*i.e.* calculated value by subtracting the dark current density) at 1.23 V (vs. the RHE) for the bare photoanode are  $17 \mu\text{A cm}^{-2}$  and  $11 \mu\text{A cm}^{-2}$ , respectively. By contrast, the overall current densities of  $\text{Ti-TiO}_{2-x}\text{@CoCr-LDH-40s}$ ,  $\text{Ti-TiO}_{2-x}\text{@NiCr-LDH-20s}$ , and  $\text{Ti-TiO}_{2-x}\text{@ZnCr-LDH-60s}$  can rise more than threefold to  $58 \mu\text{A cm}^{-2}$ ,  $67 \mu\text{A cm}^{-2}$  and  $52 \mu\text{A cm}^{-2}$ , respectively. However, the calculated photocurrent density is only slightly improved to  $14 \mu\text{A cm}^{-2}$ ,  $17 \mu\text{A cm}^{-2}$  and  $14 \mu\text{A cm}^{-2}$ , respectively, for the above three hybrid photoanodes. The majority of the overall current density increase is attributed to the dark current which was generated by the electrocatalysis of the photoanode without irradiation. These results indicate that the combination of the minor improvement from photoabsorption and the major improvement for electrocatalysis is responsible for enhancing the PEC performance of the modified photoanodes under visible light illumination.

Furthermore, the faradaic efficiency is obtained by comparing the actual  $\text{O}_2$  yield with the theoretical  $\text{O}_2$  production calculated from the photocurrent. Both the photocurrent and  $\text{O}_2$  production of the PEC water oxidation reaction were monitored during the bulk electrolysis measurements (Fig. S6†). According to Fig. S6B,† the  $\text{Ti-TiO}_{2-x}\text{@CoAl-LDH}$ ,  $\text{Ti-TiO}_{2-x}\text{@CoCr-LDH}$ , and  $\text{Ti-TiO}_{2-x}\text{@CoFe-LDH}$  hybrid photoanodes produce 40.5, 41.9 and

$34.6 \mu\text{mol O}_2$  within 5 h, which is 1.38, 1.43 and 1.18 times larger than the pristine  $\text{Ti-TiO}_{2-x}$ , respectively. The results confirm that the introduction of LDH indeed enhances the PEC water oxidation and  $\text{Ti-TiO}_{2-x}\text{@CoCr-LDH}$  has the highest PEC performance among the three hybrid photoanodes. Furthermore, the faradaic efficiency is 96.4%, 96.5%, 96.7%, and 95.1% for  $\text{Ti-TiO}_{2-x}$ ,  $\text{Ti-TiO}_{2-x}\text{@CoAl-LDH}$ ,  $\text{Ti-TiO}_{2-x}\text{@CoCr-LDH}$ , and  $\text{Ti-TiO}_{2-x}\text{@CoFe-LDH}$ , respectively, which indicates that these photoanodes are of high-efficiency for PEC water oxidation.

The stability of these four photoanodes was investigated for PEC water oxidation in Fig. S6A.† The photocurrent shows a slight decay of 2.2%, 1.6%, 1.9% and 4.5% for  $\text{Ti-TiO}_{2-x}$ ,  $\text{Ti-TiO}_{2-x}\text{@CoAl-LDH}$ ,  $\text{Ti-TiO}_{2-x}\text{@CoCr-LDH}$ , and  $\text{Ti-TiO}_{2-x}\text{@CoFe-LDH}$ , respectively, after a 5 h PEC test at 1.23 V vs. the RHE, indicating a satisfactory stability. Moreover, the  $J$ - $E$  curves of these photoanodes do not show obvious change during the 5 h test (Fig. S7A†). In addition, only a tiny change is observed in the  $\text{Ti}^{3+}$  ESR spectra of  $\text{Ti-TiO}_{2-x}$  before and after PEC measurements (Fig. S7B†), which confirms the stability of the self-doped  $\text{Ti}^{3+}$  of reduced titania during the PEC water oxidation.

### 3.4. Mechanism discussion

Based on the above results, it can be concluded that the modification of LDH co-catalysts on the surface of the reduced titania photoanode efficiently improves its PEC properties. In this section, we manage to gain a further insight into the mechanism of the PEC enhancement from both experimental measurements and theoretical calculations. The incident photon-to-current conversion efficiency (IPCE) was measured to evaluate the contributions of every incident monochromatic light with a specific wavelength for PEC performance. Fig. 7A shows the IPCEs of  $\text{Ti-TiO}_{2-x}\text{@CoAl-LDH-40s}$ ,  $\text{Ti-TiO}_{2-x}\text{@CoCr-LDH-40s}$ , and  $\text{Ti-TiO}_{2-x}\text{@CoFe-LDH-40s}$  compared with  $\text{Ti-TiO}_{2-x}$ . All the hybrid photoanodes demonstrate much higher IPCEs than the reduced titania photoanode with  $\lambda_{\text{in}} < 420$  nm. The maximum IPCEs (at 360 nm) are 80%, 81% and 79% for  $\text{Ti-TiO}_{2-x}\text{@CoAl-LDH-40s}$ ,  $\text{Ti-TiO}_{2-x}\text{@CoCr-LDH-40s}$ , and  $\text{Ti-TiO}_{2-x}\text{@CoFe-LDH-40s}$ , respectively, while only 65% is

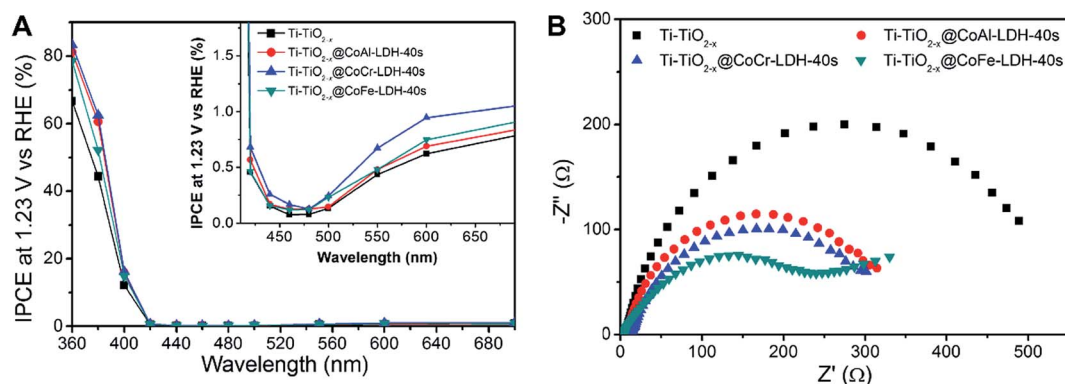


Fig. 7 (A) IPCEs measured at an applied voltage of 1.23 V (vs. the RHE), and (B) electrochemical impedance spectra (EIS) measured at the open circuit potential under illumination of the samples of  $\text{Ti-TiO}_{2-x}$ ,  $\text{Ti-TiO}_{2-x}\text{@CoAl-LDH-40s}$ ,  $\text{Ti-TiO}_{2-x}\text{@CoCr-LDH-40s}$  and  $\text{Ti-TiO}_{2-x}\text{@CoFe-LDH-40s}$ .

obtained for the unmodified Ti-TiO<sub>2-x</sub>. Meanwhile, for  $\lambda_{in} > 420$  nm, the IPCE values of hybrid photoanodes also show some slight increase relative to the reduced titania photoanode (inset of Fig. 7A). Simultaneously, similar results were also obtained for the hybrid photoanodes modified with other LDH (Fig. S8A†). The electrochemical impedance spectra (EIS) were recorded for all the photoanodes to discuss the charge transfer ability of the as-synthesized hybrid photoanodes. The smaller radius of the arcs obtained from EIS corresponds to the smaller charge transport resistance. The resulting Nyquist plots are given in Fig. 7B for Ti-TiO<sub>2-x</sub>, Ti-TiO<sub>2-x</sub>@CoAl-LDH-40s, Ti-TiO<sub>2-x</sub>@CoCr-LDH-40s, and Ti-TiO<sub>2-x</sub>@CoFe-LDH-40s. It can be clearly concluded that under illumination, the obtained radii of the arcs of Nyquist plots for the hybrid photoanodes are dramatically smaller than that of Ti-TiO<sub>2-x</sub>. This facilitates rapid separation of photo-induced electron-hole pairs and suppresses their recombination. Similar results can also be obtained for the hybrid photoanodes modified with CoZn-LDH, NiCr-LDH, ZnCr-LDH and ZnFe-LDH (Fig. S8B†).

The Mott-Schottky plots are collected in Fig. 8 to study the semiconducting properties of the samples. Taking Ti-TiO<sub>2-x</sub>@CoCr-LDH-40s as an example, obviously, the positive slope of the Mott-Schottky plots corresponds to the n-type semiconductors. Meanwhile, the slope of Ti-TiO<sub>2-x</sub>@CoCr-LDH-40s is much smaller than that of Ti-TiO<sub>2-x</sub>, which means that the former sample has a higher carrier density. Besides, this slope is the smallest among the four hybrid photoanodes, indicating that Ti-TiO<sub>2-x</sub>@CoCr-LDH-40s has the highest donor density among them. A higher donor density is beneficial for electronic conductivity within the photoanode, which can also greatly improve the efficiency of photo-generated electron-hole pair separation and transport. In addition, the flat band potential (the intercept obtained by extrapolating the Mott-Schottky plot to the horizontal axis) is related to the efficiency of electrode/electrolyte interface charge transfer ( $\eta_{transfer}$ ), and a larger flat band potential means a higher  $\eta_{transfer}$ .<sup>65</sup> Compared with Ti-TiO<sub>2-x</sub>, a slight positive shift (from 0.09 to 0.1 V) of the

flat band potential for Ti-TiO<sub>2-x</sub>@CoCr-LDH-40s is observed. Briefly, Mott-Schottky plots demonstrate both larger donor density within the bulk and favorable reaction kinetics at the interface, which are also proved by the data of hybrid photoanodes modified with other LDHs in Fig. S9.†

Density Functional Theory (DFT) was employed to investigate the band structure (Fig. S10 and S11†), band gap and band edge placement of CoAl-LDH, CoCr-LDH and CoFe-LDH by a similar method to the previous work.<sup>22</sup> The conduction band (CB) minimum and valence band (VB) maximum are determined by the band gap and work function of the semiconductor. The calculated values of the band gap and work function are 2.395 eV and 4.831 eV, 2.137 eV and 5.193 eV, 1.668 eV and 4.988 eV for CoAl-LDH, CoCr-LDH and CoFe-LDH, respectively. Accordingly, the CB minimum and VB maximum are determined to be -3.634 eV and -6.029 eV, -4.125 eV and -6.262 eV, -4.154 eV and -5.822 eV relative to the vacuum level, respectively for each kind of LDH. As a result, the schematic of band alignment between reduced titania and LDH is illustrated in Fig. 9. Obviously, the band structures of these three LDHs match well with the reduced titania for PEC water oxidation. Meanwhile, the photo-generated holes can conveniently migrate from the VB of titania to that of each LDH owing to their relative VB maximum position and the energy difference between them. This accelerated migration of holes can improve the oxygen evolution efficiency not only by the direct oxidation of water on the surface of titania but also by the oxidation of Co<sup>2+</sup> and water at the hybrid photoanode/electrolyte interface. This fast transport of holes can also facilitate the charge separation transportation, and thus suppress the charge recombination. The simulation results are consistent with the experimental results obtained by PL, PEC and IPCEs measurements. According to the literature,<sup>57,66</sup> the difference between the VB energy level maximum and the oxygen evolution redox level is the driving force for the photoinduced holes at the upper edge of the semiconductor VB to oxidize water, which suggests that the VB maximum must be more positive than the oxygen

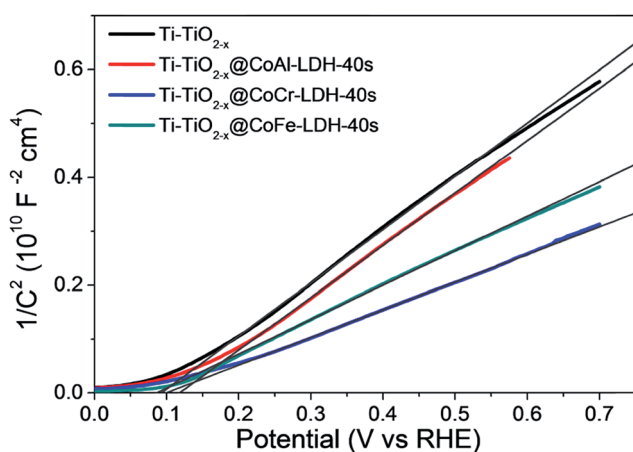


Fig. 8 Mott-Schottky plots collected at a frequency of 5 kHz in the dark for the samples of Ti-TiO<sub>2-x</sub>, Ti-TiO<sub>2-x</sub>@CoAl-LDH-40s, Ti-TiO<sub>2-x</sub>@CoCr-LDH-40s, and Ti-TiO<sub>2-x</sub>@CoFe-LDH-40s.

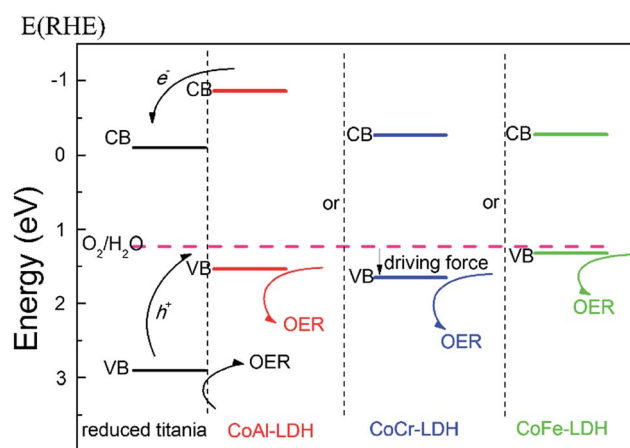


Fig. 9 Schematic of band alignment between reduced titania and LDH (i.e., CoAl-, CoCr- and CoFe-LDH) and the proposed mechanism for the enhanced PEC water oxidation performance.

redox potential in water. This driving force, combined with the bias potential, is responsible for overcoming the kinetic barrier of the OER. Herein, the driving forces of three LDHs are all positive relative to the water oxidation potential, and the values are 0.30, 0.42 and 0.09 V for CoAl-LDH, CoCr-LDH and CoFe-LDH, respectively. This shows that the CoCr-LDH has the highest driving force among them, which indicates that the lowest bias potential is needed to obtain the same current density, or the highest current density can be generated at the same bias for CoCr-LDH. These results are well supported by our PEC and IPCE results, and demonstrate the enhancement of PEC water oxidation performance for photoanodes after hybridization with LDHs.

## 4. Conclusion

In summary, we fabricated several hybrid photoanodes by integrating reduced titania with LDHs (CoAl-LDH, CoCr-LDH and CoFe-LDH). The resulting hybrid photoanode with CoCr-LDH demonstrated the highest photocurrent density, increased by 43% compared to the Ti-TiO<sub>2-x</sub> photoanode. The experiments and the DFT calculations illustrate that the band structures of these three LDHs match well with reduced titania for PEC water oxidation, and the CoCr-LDH has the highest driving force among them, which greatly improves the migration of holes from reduced titania to LDH. This facilitates the fast separation and transport of holes between the reduced titania and LDH, and thus remarkably suppresses the electron-hole recombination. In addition, the co-catalytic effect of LDH towards oxygen evolution also plays an important role in the enhancement of PEC water oxidation of the hybrid photoanodes.

## Acknowledgements

This work was supported by the National Natural Science Foundation of China (No. U1462118), the 973 Program (No. 2014CB932102), and the Fundamental Research Funds for the Central Universities (buctrc201506, PYCC1704). Partial financial support of the project from the National Science Foundation (CHE-1213795, P. F.) is also greatly appreciated.

## References

- 1 D. G. Nocera, *Acc. Chem. Res.*, 2012, **45**, 767–776.
- 2 C. Acar and I. Dincer, *Int. J. Hydrogen Energy*, 2016, **41**, 7950–7959.
- 3 Y. Izumi, *ACS Symposium Series*, American Chemical Society, Washington, DC, 2015, vol. 1194, pp. 1–46.
- 4 A. Kudo and Y. Miseki, *Chem. Soc. Rev.*, 2009, **38**, 253–278.
- 5 S. U. M. Khan, M. Al-Shahry and W. B. Ingler Jr, *Science*, 2002, **297**, 2243–2245.
- 6 J. Gong, K. Sumathy, Q. Qiao and Z. Zhou, *Renewable Sustainable Energy Rev.*, 2017, **68**, 234–246.
- 7 A. Nikokavoura and C. Trapalis, *Appl. Surf. Sci.*, 2017, **391**, 149–174.
- 8 A. H. Mamaghani, F. Haghghat and C.-S. Lee, *Appl. Catal., B*, 2017, **203**, 247–269.
- 9 A. Fujishima and K. Honda, *Nature*, 1972, **238**, 37–38.
- 10 B. Liu and E. S. Aydil, *J. Am. Chem. Soc.*, 2009, **131**, 3985–3990.
- 11 Y. J. Hwang, C. Hahn, B. Liu and P. Yang, *ACS Nano*, 2012, **6**, 5060–5069.
- 12 M. Liu, N. de Leon Snapp and H. Park, *Chem. Sci.*, 2011, **2**, 80–87.
- 13 I. S. Cho, Z. Chen, A. J. Forman, D. R. Kim, P. M. Rao, T. F. Jaramillo and X. Zheng, *Nano Lett.*, 2011, **11**, 4978–4984.
- 14 Y. J. Hwang, A. Boukai and P. Yang, *Nano Lett.*, 2009, **9**, 410–415.
- 15 P. Roy, S. Berger and P. Schmuki, *Angew. Chem., Int. Ed.*, 2011, **50**, 2904–2939.
- 16 X. Zhang, Y. Wang, B. Liu, Y. Sang and H. Liu, *Appl. Catal., B*, 2017, **202**, 620–641.
- 17 M. Xu, P. Da, H. Wu, D. Zhao and G. Zheng, *Nano Lett.*, 2012, **12**, 1503–1508.
- 18 J. H. Park, S. Kim and A. J. Bard, *Nano Lett.*, 2005, **6**, 24–28.
- 19 G. Wu, J. Wang, D. F. Thomas and A. Chen, *Langmuir*, 2008, **24**, 3503–3509.
- 20 S. Nayak, L. Mohapatra and K. Parida, *J. Mater. Chem. A*, 2015, **3**, 18622–18635.
- 21 Y. Hou, Z. Wen, S. Cui, X. Feng and J. Chen, *Nano Lett.*, 2016, **16**, 2268–2277.
- 22 F. Ning, M. Shao, S. Xu, Y. Fu, R. Zhang, M. Wei, D. G. Evans and X. Duan, *Energy Environ. Sci.*, 2016, **9**, 2633–2643.
- 23 Y. Dou, S. Zhang, T. Pan, S. Xu, A. Zhou, M. Pu, H. Yan, J. Han, M. Wei, D. G. Evans and X. Duan, *Adv. Funct. Mater.*, 2015, **25**, 2243–2249.
- 24 W. He, Y. Yang, L. Wang, J. Yang, X. Xiang, D. Yan and F. Li, *ChemSusChem*, 2015, **8**, 1568–1576.
- 25 C. Mao, F. Zuo, Y. Hou, X. Bu and P. Feng, *Angew. Chem., Int. Ed.*, 2014, **53**, 10485–10489.
- 26 F. Amano, M. Nakata, A. Yamamoto and T. Tanaka, *J. Phys. Chem. C*, 2016, **120**, 6467–6474.
- 27 D. S. Robins and P. K. Dutta, *Langmuir*, 1996, **12**, 402–408.
- 28 H. Wang, X. Xiang and F. Li, *AIChE J.*, 2009, **56**, 768–778.
- 29 G. Chen, S. Qian, X. Tu, X. Wei, J. Zou, L. Leng and S. Luo, *Appl. Surf. Sci.*, 2014, **293**, 345–351.
- 30 P. Roy Chowdhury and K. G. Bhattacharyya, *RSC Adv.*, 2015, **5**, 92189–92206.
- 31 M. Laipan, R. Zhu, J. Zhu and H. He, *J. Mol. Catal. A: Chem.*, 2016, **415**, 9–16.
- 32 Y. Ao, D. Wang, P. Wang, C. Wang, J. Hou and J. Qian, *Mater. Res. Bull.*, 2016, **80**, 23–29.
- 33 M. Dinari, M. M. Momeni and Y. Ghayeb, *J. Mater. Sci.: Mater. Electron.*, 2016, **27**, 9861–9869.
- 34 L. Mohapatra and K. M. Parida, *Phys. Chem. Chem. Phys.*, 2014, **16**, 16985–16996.
- 35 C. G. Silva, Y. Bouizi, V. Fornes and H. Garcia, *J. Am. Chem. Soc.*, 2009, **131**, 13833–13839.
- 36 Y. Lee, J. H. Choi, H. J. Jeon, K. M. Choi, J. W. Lee and J. K. Kang, *Energy Environ. Sci.*, 2011, **4**, 914–920.
- 37 B. Li, Y. Zhao, S. Zhang, W. Gao and M. Wei, *ACS Appl. Mater. Interfaces*, 2013, **5**, 10233–10239.

- 38 Y. Zhao, B. Li, Q. Wang, W. Gao, C. J. Wang, M. Wei, D. G. Evans, X. Duan and D. O'Hare, *Chem. Sci.*, 2014, **5**, 951–958.
- 39 S. J. Kim, Y. Lee, D. K. Lee, J. W. Lee and J. K. Kang, *J. Mater. Chem. A*, 2014, **2**, 4136–4139.
- 40 G. Chen, Y. Zhao, L. Shang, G. I. Waterhouse, X. Kang, L. Z. Wu, C. H. Tung and T. Zhang, *Adv. Sci.*, 2016, **3**, 1500424.
- 41 K. Parida and L. Mohapatra, *Dalton Trans.*, 2012, **41**, 1173–1178.
- 42 J. L. Gunjekar, T. W. Kim, H. N. Kim, I. Y. Kim and S. J. Hwang, *J. Am. Chem. Soc.*, 2011, **133**, 14998–15007.
- 43 J. L. Gunjekar, I. Y. Kim, J. M. Lee, N.-S. Lee and S.-J. Hwang, *Energy Environ. Sci.*, 2013, **6**, 1008–1017.
- 44 S. Xia, L. Zhang, X. Zhou, G. Pan and Z. Ni, *Appl. Clay Sci.*, 2015, **114**, 577–585.
- 45 Y. Fu, F. Ning, S. Xu, H. An, M. Shao and M. Wei, *J. Mater. Chem. A*, 2016, **4**, 3907–3913.
- 46 M. Shao, F. Ning, M. Wei, D. G. Evans and X. Duan, *Adv. Funct. Mater.*, 2014, **24**, 580–586.
- 47 C. Zhang, M. Shao, F. Ning, S. Xu, Z. Li, M. Wei, D. G. Evans and X. Duan, *Nano Energy*, 2015, **12**, 231–239.
- 48 D. Xu, Y. Rui, Y. Li, Q. Zhang and H. Wang, *Appl. Surf. Sci.*, 2015, **358**, 436–442.
- 49 D. H. Youn, Y. B. Park, J. Y. Kim, G. Magesh, Y. J. Jang and J. S. Lee, *J. Power Sources*, 2015, **294**, 437–443.
- 50 J. Huang, G. Hu, Y. Ding, M. Pang and B. Ma, *J. Catal.*, 2016, **340**, 261–269.
- 51 L. Wang, F. Dionigi, N. T. Nguyen, R. Kirchgeorg, M. Gliech, S. Grigorescu, P. Strasser and P. Schmuki, *Chem. Mater.*, 2015, **27**, 2360–2366.
- 52 H. Qi, J. Wolfe, D. Fichou and Z. Chen, *Sci. Rep.*, 2016, **6**, 30882.
- 53 T. Kameyama, K. Okazaki, K. Takagi and T. Torimoto, *Phys. Chem. Chem. Phys.*, 2009, **11**, 5369–5376.
- 54 Y. Tang, R. Wang, Y. Yang, D. Yan and X. Xiang, *ACS Appl. Mater. Interfaces*, 2016, **8**, 19446–19455.
- 55 W. He, R. Wang, L. Zhang, J. Zhu, X. Xiang and F. Li, *J. Mater. Chem. A*, 2015, **3**, 17977–17982.
- 56 C. Li, M. Wei, D. G. Evans and X. Duan, *Small*, 2014, **10**, 4469–4486.
- 57 S.-M. Xu, T. Pan, Y.-B. Dou, H. Yan, S.-T. Zhang, F.-Y. Ning, W.-Y. Shi and M. Wei, *J. Phys. Chem. C*, 2015, **119**, 18823–18834.
- 58 Z. Zhang, M. N. Hedhili, H. Zhu and P. Wang, *Phys. Chem. Chem. Phys.*, 2013, **15**, 15637–15644.
- 59 Y. Zhao, C. J. Wang, W. Gao, B. Li, Q. Wang, L. Zheng, M. Wei, D. G. Evans, X. Duan and D. O'Hare, *J. Mater. Chem. B*, 2013, **1**, 5988–5994.
- 60 G. Wang, H. Wang, Y. Ling, Y. Tang, X. Yang, R. C. Fitzmorris, C. Wang, J. Z. Zhang and Y. Li, *Nano Lett.*, 2011, **11**, 3026–3033.
- 61 Y. Mi and Y. Weng, *Sci. Rep.*, 2015, **5**, 11482.
- 62 Y. Wang, H. Zhang, P. Liu, X. Yao and H. Zhao, *RSC Adv.*, 2013, **3**, 8777–8782.
- 63 J. C. Yu, J. Yu, W. Ho, Z. Jiang and L. Zhang, *Chem. Mater.*, 2002, **14**, 3808–3816.
- 64 X. G. Zhao and L. Q. Huang, *Ceram. Int.*, 2017, **43**, 3975–3980.
- 65 W. Li, P. Da, Y. Zhang, Y. Wang, X. Lin, X. Gong and G. Zheng, *ACS Nano*, 2014, **8**, 11770–11777.
- 66 A. Valdes, Z.-W. Qu, G.-J. Kroes, J. Rossmesl and J. K. Nørskov, *J. Phys. Chem. C*, 2008, **112**, 9872–9879.